J Fluoresc (2014) 24:1253–1262
DOI 10.1007/s10895-014-1409-9

ORIGINAL PAPER

# Influence of Surface Coating on Structural and Photoluminescent Properties of $CaMoO_4$:Pr Nanoparticles

**Anees A. Ansari · A. K. Parchur · M. Alam · J. Labis · Abdallah Azzeer**

Received: 1 April 2014 / Accepted: 19 May 2014 / Published online: 29 May 2014


**Abstract** $CaMoO_4$:Pr(core), $CaMoO_4$:Pr@$CaMoO_4$ (core/shell) and $CaMoO_4$:Pr@$CaMoO_4$@$SiO_2$ (core/shell/shell) nanoparticles were synthesized using polyol method. X-ray diffraction (XRD), thermogravimatric analysis (TGA), UV–vis absorption, optical band gap energy analysis, Fourier transform infrared (FTIR), FT-Raman and photoluminescence (PL) spectroscopy were employed to investigate the structural and optical properties of the synthesized core and core/shell nanoparticles. The results of the XRD indicate that the obtained core, core/shell and core/shell/shell nanoparticles crystallized well at ~150 °C in ethylene glycol (EG) under urea hydrolysis. The growth of the $CaMoO_4$ and $SiO_2$ shell (~12 nm) around the $CaMoO_4$:Pr core nanoparticles resulted in an increase of the average size of the nanopaticles as well as in a broadening of their size distribution. These nanoparticles can be well-dispersed in distilled water to form clear colloidal solutions. The photoluminescence spectra of core, core/shell and core/shell/shell nanoparticles show the characteristic charge transfer emission band of $MoO_4^{2-}$ (533 nm) and $Pr^{3+}$ $4f^2 \rightarrow 4f^2$, with multiple strong $^3H_4 \rightarrow {}^3P_2$, $^1D_2 \rightarrow {}^3H_4$ and $^3P_0 \rightarrow {}^3F_2$ transitions located at ~490, 605 and 652 nm, respectively. The emission intensity of the $CaMoO_4$:Pr@$CaMoO_4$ core/shell and $CaMoO_4$:Pr@$CaMoO_4$@$SiO_2$ core/shell/shell nanoparticles increased ~4.5 and 1.7 times,respectively, with respect to those of $CaMoO_4$:Pr core nanoparticles. This indicates that a significant amount of nonradiative centers existing on the surface of $CaMoO_4$:Pr@$CaMoO_4$ core/shell nanoparticles can be eliminated by the shielding effect of $CaMoO_4$ shells.

**Keyword** Calcium molybdate nanoparticles · Absorption spectra · Band gap energy · Photoluminescence

A. A. Ansari (✉) · J. Labis · A. Azzeer
King Abdullah Institute for Nanotechnology, King Saud University, P.O. Box 2455, Riyadh 11451, Saudi Arabia
e-mail: aneesaansari@gmail.com

A. K. Parchur
Department of Physics, Banaras Hindu University, Varanasi 221005, India

M. Alam
Research Center, College of Science, King Saud University, P.O. Box 2455, Riyadh, Saudi Arabia

## Introduction

Presently, rare-earth ions-doped oxides have been extensively studied because of their interesting luminescence properties [1–3]. Rare- earth Praseodymium (Pr) is a very attractive activator, because it contains several metastable multiplets, which can lead to a variety of emissions right from the blue to the red and infrared wavelengths, which is of great importance for luminescent devices, especially in modern display technologies like field-emission displays [4–8]. On the other hand, calcium molybdate ($CaMoO_4$) is an excellent luminescent host material and solid-state lasers materials because of its high radiative emission rate, broad emission band in visible region and refractive index [9–11]. Calcium molybdate has a scheelite-type crystalline structure (tetragonal symmetry $C_{4h}^6$) with wide band gap semiconductor of 3.6 eV, which makes it possible to incorporate luminescent centers of various rare-earth activator ions [9–11]. This material attracts great attention due to its property of producing green luminescence; hence, it covers a wide variety of technical applications of $CaMoO_4$ in opto-electronics, bio-photonics, solid state laser and biomedical applications. Moreover, as observed in literature, $CaMoO_4$ nanophosphor exhibits higher light-emitting efficiency and better color purity as compared to other commercial phosphors [11]. Owing to their strong broad emission band in visible region, high chemical and thermal stability, $CaMoO_4$ nanophosphor can be used for medical diagnostics and in nano-biotechnology applications such as bio labeling, bioimaging [11, 12].

In terms of optical properties, calcium molybdate exhibits green and/or blue luminescence emissions at room temperature when excited with wavelengths in the range from 240 to 537 nm. Recently, $CaMoO_4$ have been synthesized by many researchers and their structural and their optical properties have been investigated [13–17]. For example, Mikhailik et al. explained that the short wavelength luminescence of this molybdate is usually caused by the intrinsic emission of the $[MoO_4]^{2-}$molecular complexes while its long wavelength luminescence arises from the $MoO_3$ oxygen deficient defect centers [18]. In another work Mikhailik et al. investigated the electronic transitions and luminescence decay kinetics of $CaMoO_4$ at low temperatures by means of ultraviolet excitation [19]. Chung et al., prepared the $Li^+/Tm^{3+/}Yb^{3+}$ co-doped $CaMoO_4$ upconversion phosphor by complex citrate-gel method and investigated their upconversion luminescence properties [20]. Marques et al., investigated the effect of different solvent rations on the growth of $CaMoO_4$ and measured theUV/Vis absorption spectra as a evidence in variation of optical band gap values for the distinct morphologies [9] . In other report, Longo et al., have observed strong greenish-light photoluminescence (PL) emission at room temperature for disordered and ordered powders of $CaMoO_4$ prepared by polymeric precursor method [10]. However, due to the nonradiative decay from the defects on the surface of the nanoparticles, the luminescence efficiency of nanostructural materials is usually lower than that of the corresponding bulk materials. To reduce these defects, the growth of a crystalline shell of a suitable inorganic material around each nanocrystal to form the core-shell structures has been regarded as an effective strategy to improve luminescent efficiency.

In this paper, we report the synthesis of $CaMoO_4$:Pr core nanoparticles by polyol method under urea thermal decomposition at 150 °C. These core nanoparticles were coated with crystalline $CaMoO_4$ layer and thereafter with amorphous silica shell around the surface of core nanoparticles. These core and core-shell nanoparticles were analyzed by X-ray diffraction (XRD), thermogravimatric analysis (TGA), UV–vis absorption spectra, optical band gap energy, Fourier transform Raman (FT-Raman) spectroscopy, Fourier transform infrared (FT-IR) spectroscopy and photoluminescence(PL) measurements. In addition, the structure, optical properties and thermal stability of the synthesized nanophosphors are also systematically studied in this article.

## Experimental

### Chemicals

Praseodymium oxide (99.99 %, Alfa Aesar, Germany), calcium carbonate ($CaCO_3$, 99.99 %, E-Merck, Germany), Ammonium molybdate($(NH_4)_6Mo_7O_{24}\cdot 4H_2O$,99.3 %, Acros Organics), Tetraethyl-orthosilicate (TEOS, 99 wt% analytical reagent A.R.), ethylene glycol(EG; E-Merck, Germany), Urea$(NH_2)_2CO$; E-Merck, Germany), $C_2H_5OH$, $HNO_3$ and $NH_4OH$ were used as starting materials without any further purification. Nanopure water was used for preparation of solutions. The ultrapure de-ionized water was obtained using a Milli-Q system (Millipore, Bedford, MA, USA). All other chemicals used were of reagent-grade.

### Preparation of $CaMoO_4$:Pr Nanoparticles (Core)

For typical preparation of $Pr^{3+}$ doped $CaMoO_4$ nanoparticles, ~0.692 g of $CaCO_3$ and 0.0614 g of $Pr_4O_7$ were dissolved together in conc. nitric acid ($HNO_3$) and heated upto 80 °C to remove excess acid and neutralized by addition of double distilled water. 1.246 g ammonium molybdate dissolved in methanol (50 ml) was mixed in this foregoing reaction and kept for constant stirring with heating (80 °C) on hot plate for 1 h. 2.0 g urea dissolved in 50 ml EG was introduced into this reaction. The reaction mixture was heated upto ~150 °C for 3 h under reflux conditions until the white precipitate was appeared. The synthesized product precipitate was then collected by centrifugation, washed with distilled water and absolute ethanol 5 times, and dried in oven at ~200 °C for 6 h for characterization.

### Preparation of $CaMoO_4$:Pr@$CaMoO_4$ Core-Shell Nanoparticles (Core/Shell)

For the preparation of $CaMoO_4$:Pr@$CaMoO_4$ core-shell nanoparticles, similar polyol process was used as discussed above. 1.00 g of $CaMoO_4$:Pr were dispersed in 25 ml of distilled water containing 1 g of EG and 2 g urea with constant stirring for 30 min. Typically ~0.703 g $CaCO_3$ was dissolved in $HNO_3$ acid and the excess amount of nitric acid is evaporated on hot plate by adding double distilled water. Then a solution of calcium carbonate and 1.265 gm ammonium molybdate dissolved in methanol was injected into the foregoing mixed system, and the suspension was refluxed at ~150 °C for 3 h until the precipitation is occurred. This white precipitate was centrifuged and washed many times with methanol to remove excess unreacted reactants. The core-shell nanoparticles were collected after centrifugation and allowed to dry in ambient temperature for characterization.

### Preparation of Silica Coated $CaMoO_4$:Pr@$CaMoO_4$@$SiO_2$ Core-Shell Nanoparticles (Core/Shell/Shell)

$CaMoO_4$:Pr@$CaMoO_4$@$SiO_2$ core-shell nanoparticles were prepared through a versatile solution sol–gel method as follows [21]. The synthesized $CaMoO_4$:Pr@$CaMoO_4$ nanoparticles (50 mg) were well-dispersed in a mixed solution of deionized water (50 mL), ethanol (70 mL) and conc. aqueous

ammonia (1.0 mL) in a three-neck round-bottom flask. Afterwards, 2.0 mL of tetraethyl orthosilicate (TEOS) was added drop-wise in 2 min, and the reaction was allowed to proceed for 3–4 h under continuous mechanical stirring. After 3 h of continuous stirring at room temperature, the silica-coated $CaMoO_4$:Pr@$CaMoO_4$ core-shell nanoparticles were separated by centrifugation, washed several times with ethanol and dried at room temperature.

### Characterization Methods

The X-ray diffraction (XRD) of the powder samples was examined at room temperature with the use of PANalytical X'Pert X-ray diffractometer equipped with a Ni filtered using Cu $K_\alpha$ ($\lambda$=1.54056 Å) radiations as X-ray source. The nanoparticles were characterized using a JEOL JEM-2,100 F Transmission Electron Microscope (TEM) at an accelerating voltage of 200 keV. Samples were mounted on a 300 mesh size lacey carbon coated TEM grid. 5 mg of nanoparticles were dispersed in 20 ml if distilled water and ultrasonicated for about 30 min. A drop of dispersed nanoparticles is placed onto a copper grid and allowed to dry at ~50 °C for 30 min. such grids are used for bright field TEM imaging and selected area electron diffraction (SAED). Raman spectra were recorded on a Jobin Yvon Horiba HR800 UV Raman microscope using a HeNe laser emitting at 632.8 nm. The UV/Vis absorption spectra were measured a Perkin-Elmer Lambda-40 spectrophotometer, with the sample contained in 1 $cm^3$ stoppered quartz cell of 1 cm path length, in the range 190–600 nm. TGA was performed with TGA/DTA, Mettler Toledo AG, Analytical CH-8603, Schwerzenbach, Switzerland. The FTIR spectra were recorded on a Perkin-Elmer 580B IR spectrometer using KBr pellet technique in the range 4,000–400 $cm^{-1}$. The PL spectra were recorded on Horiba Synapse 1024× 256 pixels, size of the pixel 26 microns, detection range: 300 (efficiency 30 %) to 1,000 nm (efficiency:35 %). A slit width of 100 μm was employed, ensuring a spectral resolution better than 1 $cm^{-1}$. All measurements were performed at room temperature.

## Results and Discussion

Figure 1 shows the crystal phase analysis of $Pr^{3+}$ doped $CaMoO_4$ (core) and their $CaMoO_4$ and $SiO_2$-shell modified nanoparticles. All diffraction peaks are indexed to the tetragonal scheelite structure with cell parameters of $a$=5.19 Å and $c$=11.25 Å (JCPDS card No. 29–0351)[9–11]. No impurity peaks are detected even after shell formation in the experimental range, thus indicating the formation of pure $CaMoO_4$ nanoproducts. The lattice parameters calculated for core,

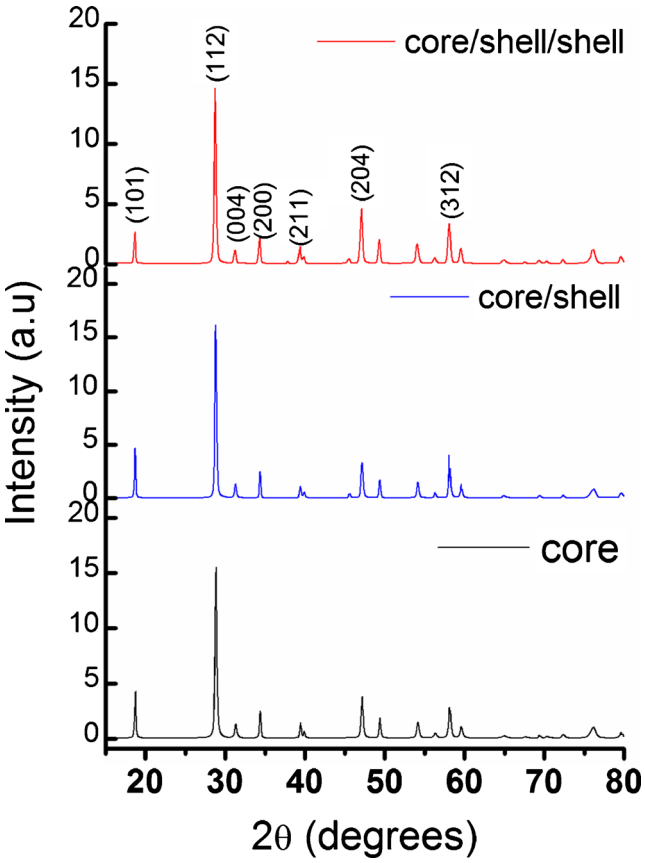


**Fig. 1** XRD patterns of $CaMoO_4$:Pr (core), $CaMoO_4$:Pr@$CaMoO_4$ (core/shell), $CaMoO_4$:Pr@$CaMoO_4$@$SiO_2$ (core/shell/shell) nanoparticles

core/shell and core/shell/shell nanoparticles are found to be $a$=~5.212 Å, $c$=11.418 Å and $V$=310.18 $Å^3$, $a$=5.218 Å, $c$=11.423 Å and $V$=311 $Å^3$, and $a$=5.217 Å, $c$=11.438 Å and $V$=311.34 $Å^3$, respectively. The XRD pattern profile intensity of core, core/shell and core/shell/shell nanoparticles is found to be 100, 94 and 87 %, respectively. There is significant difference in diffraction peak intensity of $SiO_2$ shell formed over core/shell nanoparticles. Moreover, doping of $Pr^{3+}$ ions and/or shell formation have slight effect on the crystallinity of the nanoparticle due to high surface defects. The results are in good agreement with the published literature reports [9–11]. These results indicate that the core, core/shell and core/shell/shell nanoparticles are highly crystalline, pure and ordered at long range. The average crystallite size from the XRD patterns is used to calculate using Scherrer relation, which is expressed as;

$$D = \frac{0.89\lambda}{\beta_{hkl}\, Cos(\theta)} \quad (1)$$

where λ is the wavelength of the X-rays and $\beta_{hkl}$ the full width at half maximum (FWHM) of the peak in the XRD pattern. Its values are found to be ~31.5, 34.5 and 36 nm for

core, core/shell and core/shell/shell nanoparticles, respectively. The increase in crystallite size of core/shell and core/shell/shell nanoparticles as compared to core is due to the surface coating over core nanoparticles. To the best of our knowledge, this is the first report on synthesis of $CaMoO_4$:Pr, $CaMoO_4$:Pr@$CaMoO_4$ and $CaMoO_4$:Pr@$CaMoO_4$@$SiO_2$ core/shell nanoparticles produced through a facile polyol synthesis.

The size and morphology of the core, core/shell and core/shell/shell nanoparticles was analyzed by TEM images and shown in Fig. 2a, b and c. From the low magnification TEM micrograph (Fig. 2a), it can be seen, that the as-prepared $CaMoO_4$:Pr sample is consists of aggregated spherical with polycrystalline nanosized particles morphology, and average particles size of the material is in between ~15–50 nm. The selected area electron diffraction (SAED) can be can be indexed to a pure tetragonal phase (scheelite). The appearance of periodic diffraction spots indicates that these nanostructures are self-assembled into highly oriented aggregates and diffract as a single crystal (see inset of Fig. 2a). The clearly resolved lattice fringes are 0.25 nm, corresponding to the (200) plane of tetragonal $CaMoO_4$, which is in accordance with the SAED result (shown in inset of Fig. 2a). The corresponding SAED pattern (Fig. 2a) thus confirms that the structure has morphology of the polycrystalline particles. As seen in Fig. 2b, the core/shell nanoparticles are highly agglomerated with different particle size distribution. In this micrograph, the dark areas are related to the high concentration of small particles with aggregate nature. Cavalcante et al., observed that the PEG promote the increase in aggregation process of small particles or nucleation seeds on the surface through the lateral interaction of hydrogen bonding of water with the -OH groups of this polymer [22]. From the TEM micrographs for the core and core/shell nanoparticles (Fig. 2a and b), we observed that the prepared nanocrystals are in irregular in shapes and sizes, which are highly aggregated with narrow size distribution. Silica surface modification is performed over core/shell nanoparticles and the particles are still aggregated with irregular size distribution. But these nanoparticles are considerably larger in size (~50–180 nm) than the core particles size. This is caused by the coating of nonporous silica through a sol–gel process, as shown in Fig. 2c. An average ~12 nm thickness of $SiO_2$ shell is coated over core/shell nanoparticles (Inset of Fig. 2c). The luminescent cores are dark black irregular shape with an average size of about 150–200 nm. Interestingly, silica coated core-shell nanoparticles did not exhibit smooth surface. This confirms that the irregular shape of the nanoparticles was synthesized by co-precipitation process. Figure 2d shows the energy dispersive X-ray spectrograph of core samples. It shows the presence of different ions present in the samples, which are assigned in the figure itself. $Pr^{3+}$ ion peak at ~5.32 eV is very small as compared to other elements and this is may be due to the presence of small amount of ions in the sample.

Thermogravimatric analysis was employed to examine the thermal stability, nature of coordinated water and organic moiety molecules on the surface of as-prepared core, core/shell and core/shell/shell nanoparticles between the

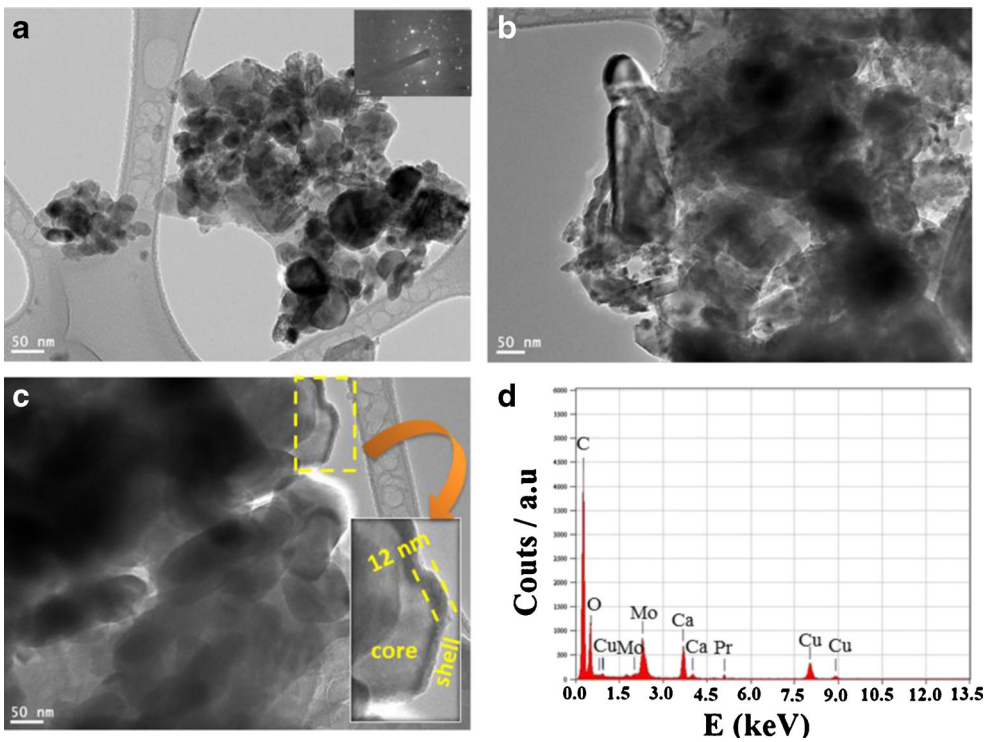


**Fig. 2** TEM images of (**a**) $CaMoO_4$:Pr (core), Inset shows the SAED patterns, (**b**) $CaMoO_4$:Pr@$CaMoO_4$ (core/shell) (**c**) $CaMoO_4$:Pr@$CaMoO_4$@$SiO_2$ (core/shell/shell) nanoparticles. Inset of (c) shows the expansion to the edge of particle showing silica shell coating of thickness ~12 nm and (d) EDX of (a)

temperature ranges of ~25–800 °C under a nitrogen atmosphere with a heating rate of 10 °C/min. Figure 3 display that all thermograms are stable and do not show any weight loss up to 300 °C, it supports that samples are devoid of lattice as well as coordinated water or organic molecules. The thermograms of core and core-shell nanoparticles are similar in shape and show degradation of their constituents into decomposition step. There is ~1.1–1.3 % weight loss upto 500 °C (core and core/shell) whereas core/shell/shell nanoparticles show 1.7 % loss, which is slightly higher than that of the core and core/shell nanoparticles. An average thermogram for core, core/shell and core/shell/shell nanoparticles exhibits a minor weight loss (3 %) between 300 and 800 °C, and corresponds to the burning and elimination of carbonates linked with molybdenum. After 800 °C, no obvious weight loss is observed., whereas, this weight loss is higher in $CaMoO_4$:Pr@$CaMoO_4$@$SiO_2$ core/shell/shell nanoparticles, It is due to the burning of amorphous silica, slowly is eliminating silica and thus transforming into silicate.

The optical absorption spectra for core, core/shell and core/shell/shell nanoparticles dispersed in distilled water are recorded over the 200–800 nm UV/Vis spectral region and shown in Fig. 4. The absorption spectrum of $CaMoO_4$:Pr exhibits typical optical behavior of a wide band gap semiconducting oxide, having an intense absorption band between ~250–300 nm with a steep edge [15]. The sharp spectrum with high absorbance in the UV region indicates the formation of a stable colloidal solution. It is observed that the optical absorption spectra of the as-prepared $CaMoO_4$:Pr nanoparticles is closely similar to that ($\lambda_{max}$=250–300 nm) of the reported $CaMoO_4$ nanoparticles [23]. This is a fundamental transition which is attributed to the charge transfer transition from the oxygen ligand (2*p*) to the central molybdenum atom inside the $[MoO_4]^{2-}$ ion [9–11, 15, 23]. The absorption bands

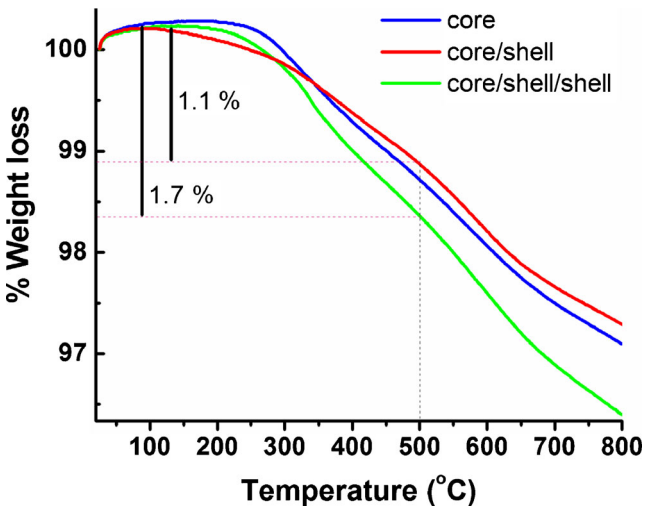


**Fig. 3** TGA curves (weight loss) for (**a**) $CaMoO_4$:Pr (core) (**b**) $CaMoO_4$:Pr@$CaMoO_4$ (core/shell) (**c**) $CaMoO_4$:Pr@$CaMoO_4$@$SiO_2$ (core/shell/shell) nanoparticles

for trivalent praseodymium ion corresponding to the forbidden 4*f*–4*f* electronic transitions, such as $^3H_4 \rightarrow {}^1D_2$, $^3H_4 \rightarrow {}^3P_2$, $^3H_4 \rightarrow {}^3P_1 + {}^1I_6$ and $^3H_4 \rightarrow {}^3P_0$, are not detected, and could be due to low quantity of $Pr^{3+}$ and/or high absorbance of charge transfer transition in the same visible region [24] . The appearance of an additional broad band for core/shell/shell ($CaMoO_4$:Pr@$CaMoO_4$@$SiO_2$) nanoparticles with peak maxima at 287 nm, originates from the silica [25] and/or $[MoO_4]^{2-}$ ion. It indicates a successful coating of silica around the surface of nanoparticle (~12 nm). This absorption band of silica is in agreement with other literature reports [2, 21]. It is also observed that silica surface modified nanoparticles exhibit good solubility in water accompanied by a strong decrease of their solubility in organic solvents. As discussed and reported from other literatures, the broad size distribution of the nanoparticles derived from the optical absorption studies is ideal for bio-tagging experiments, because bio-tagging experiments will always be performed in solution [2, 12, 21].

The electronic band structure in which the band gap energy (Eg) is estimated from the energy difference between the highest occupied molecular orbital (HOMO) and the lowest unoccupied molecular orbital (LUMO). In both crystalline and amorphous materials, the absorption coefficient near the fundamental absorption edge is dependent on photon energy.

In the high-absorption region, the dependence of the absorption coefficient on photon energy is expressed by Tauc's equation, as in Eq. (3) [26]

$$(\alpha h\nu) = \beta\left(h\nu - E_g\right)^{m} \tag{2}$$

where β is an energy-independent constant, α the optical absorption coefficient, *h* the Planck constant, ν the frequency of incident photon, $E_g$ the optical bandgap, and m is a constant that characterizes the nature of the band transition. The values for $m$=1/2 and 3/2 corresponds to direct allowed and direct forbidden transitions, respectively, whereas $m$=2 and 3 corresponds to indirect allowed and indirect forbidden transitions, respectively. The band gap can also be obtained by the extrapolation of the straight-line portion of the $(\alpha h\nu)^{1/m}$ versus $h\nu$ plot to $h\nu$=0.

Accordingly, the bandgap energy calculated (Fig. 4) from Tauc's plot varies from to 4.9–5.3 eV [26]. This value is higher than those earlier reported theoretically and experimentally by many researchers for a well-ordered $CaMoO_4$ crystal [9, 10, 15, 23]. Table 1 shows a comparative analysis between $E_g$ values of $CaMoO_4$ obtained in this work with those reported in the literature by different methods [27, 28]. The differences verified in the optical band gap values can be related to the different preparation methods, shape, average crystal size and structural order–disorder degree in the lattice. As seen in insets of Fig. 4, the $E_g$ values for core, core/shell and core/shell/shell nanoparticles are found to be ~5.1, 5.3 and 4.9 eV, respectively. These results reveal that the value of $E_g$

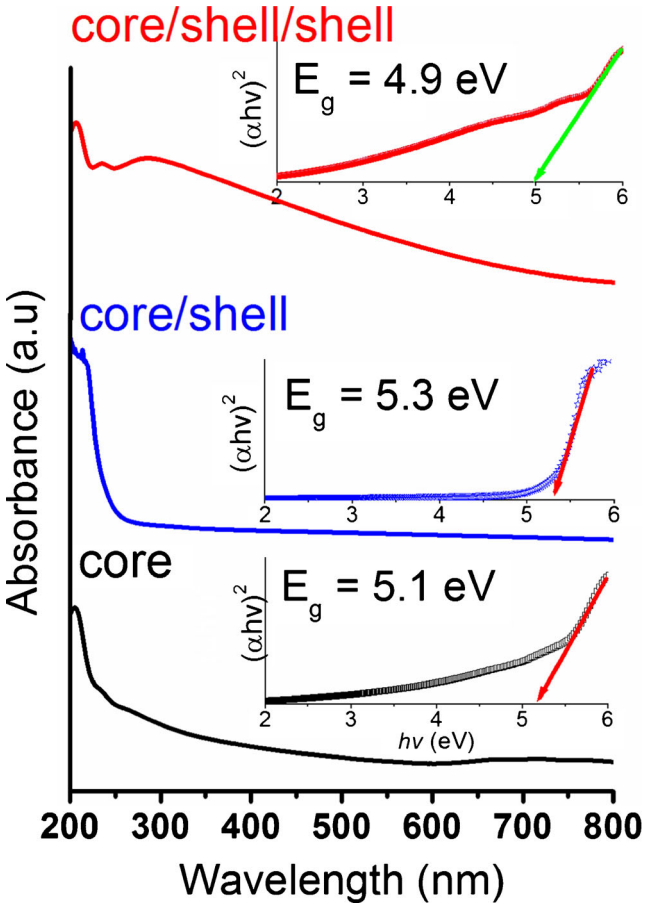


**Fig. 4** UV–vis absorption spectrum of $CaMoO_4$:Pr (core), $CaMoO_4$:Pr@$CaMoO_4$ (core/shell) and $CaMoO_4$:Pr@$CaMoO_4$@$SiO_2$ (core/shell/shell) nanoparticles. The band gap of corresponding samples is shown in figure inset itself

depends on the crystallite size. It is therefore suggested that the values of $E_g$ varies depending on crystallite size. These results are verified from the XRD results, suggesting the decrease in reflection peaks intensity after shell formation. Owing to the shell formation then, crystallinity decrease because of the increase the particle size.

Figure 5 displays comparative FTIR absorption spectral analysis of core, core/shell and core/shell/shell nanoparticles recorded at room temperature. The $Pr^{3+}$ ion-doped $CaMoO_4$ presents a scheelite-type tetragonal structure in good agreement with XRD patterns and FT-Raman spectra (Figs. 1 and 6). The tetrahedral symmetry is represented by: $\Gamma_{Td}=A_1(\nu_1)+E(\nu_2)+F_2(\nu_3)+F_2(\nu_4)$, but only the $F_2(\nu_3, \nu_4)$ modes are active in infrared. The $F_2(\nu_3)$ vibrations are antisymmetric stretches, whereas the $F_2(\nu_4)$ vibrations are bending modes [9, 15]. The bands at 825 and 432 $cm^{-1}$ are assigned to asymmetric stretching and bending vibrations of $MoO_4^{2-}$ tetrahedron, respectively. Inset shows the expansion to the spectra between 460 and 410 $cm^{-1}$. There is a slight shifting of ~2 $cm^{-1}$ is observed on core/shell formation. A strong band between 900 and 600 $cm^{-1}$ are assigned to $F_2(\nu_3)$ asymmetric stretching vibrations of O-Mo-O bonds into the $MoO_4^{2-}$ tetrahedron molecule. These observed bands are broad and sharp for the core/shell/shell nanoparticles due to the characteristic vibrational bands of Si–O, Si–OH, Si–O–Si, resulting from successful silica surface modification [2]. An infrared weak band is observed for $CaMoO_4$:Pr nanoparticles at 3,423 and 1,623 $cm^{-1}$, and can be ascribed to O–H stretching vibration and H–O–H bending vibration of the physically adsorbed water molecules on the nanoparticle surface [2]. These bands are diminished for core and core/shell nanoparticles because of anhydrous nature of the products. These results are in good agreement with the TGA analysis.

Figure 6 exhibits the normalized Raman scattering spectra of core, core/shell and core/shell/shell nanoparticles recorded at room temperature. The inset shows the expansion to the Raman spectra between 100–450 and 860–890 $cm^{-1}$. According to the literature reports, the primitive cell of $CaMoO_4$ includes two formulaic units; the $[MoO_4]^{2-}$ ionic group with strong covalent Mo–O bonds ($T_d$ symmetry) and the $Ca^{2+}$ cations [9, 15]. As illustrated in Fig. 6, only 7 Raman-active modes were detected, the other ($1B_g$ and $1E_g$) vibration modes were not detectable, probably due to their low intensities. The strong and intense Raman peaks that appeared at 321, 391, 791, 844 and 877 $cm^{-1}$ are attributed to the $\nu_2A_g$, $\nu_2E_g$, $E_g$, $B_g$ and $A_g$ modes indicative of internal $MoO_4$ vibrations in crystalline $CaMoO_4$:Pr sample. The external modes involve the movementof $MoO_4$ ions as a whole, which are only weakly coupled with $Ca^{2+}$ cations. Hence, the external modes $2B_g$ and $1E_g$ are assigned to the lowest-frequency band, i.e. at 85 $cm^{-1}$. Moreover, the Raman spectra exhibited intense and broad bands, indicating a strong interaction between the O-Ca-O and O-Mo-O bonds in the clusters. The positions of each Raman-activemode are listed in Table 2. A closer analysis of the results displayed in this table indicated that the relative positions of all Raman-active modes for core, core/shell and core/shell/shell nanoparticles reported in this work are in good agreement with those previously reported in the literature [9, 15]. The small shifts observed in the positions of Raman modes can arise from different factors such as the preparation method, the average crystal size, the interaction forces between ions, and the degree of structural order in the lattice.

The emission specra was recorded to investigate the photoluminescence properties of the as-prepared nanophosphors. Figure 7a shows emission spectra measured at room temperature for the core, core/shell and core/shell/shell nanoparticles excited by the 325 nm line of a He:Cd laser. The nanophosphor spectra present a broad band covering the visible electromagnetic spectra in the range from 375 to 800 nm, and the profile of the emission band is typical of a multiphonon and multilevel process, that is, a system in which relaxation occurs by several paths involving the participation of numerous states within the band gap of the material [9, 11]. Calcium molybdate is a well-known host

**Table 1** Comparative results between the optical band gap energy of $CaMoO_4$ obtained in this work and those reported in the literature

| Methods | Particle size | $E_{gap}$ (eV) | Reference |
|---|---|---|---|
| Polymeric precursor method | 70–251*nm* (TEM) | 4.0 | Longo et al., 2008 |
| Combustion process | 25 nm(XRD) | 3.72 | Vidya et al.,2012 |
| Citrate complex route | 20~30 nm (TEM) | 4.7 eV | Yoon et al., 2011 |
| Coprecipitation method | 1.25 to 4.75 μm(TEM) | 3.68–3.44 | Marques et al.,2010 |
| Microwave-hydrothermal method | 50–61 nm (SEM) | 3.4–3.97 | Longo et al., 2011 |
| Citrate complex polymerization | 25–53 nm (XRD) | 4.87 to 5.18 | Marques et al., 2008 |
| Polyol thermal decomposition of urea | 31–36 nm (XRD) | 5.3 | Present work |

material, it exhibits a broad PL greenish emission band in visible region centered at ~534 nm, which is closely similar to the published reports [9–11, 15–17]. Moreover, its position varies depending on particle size. Several hypotheses are reported in the literature to explain the possible mechanisms responsible for the PL emission of $CaMoO_4$. As seen in Fig.7a the emission intensities for the observed samples were quite different. It suggests the change in emission intensity related to the surface properties and as well as particle size of the as-prepared nanophosphor samples. It should be noted that the emission intensity of core/shell/shell nanoparticles obviously decreases in comparison with that of the core/shell sample. It is observed that the surface coating of the core nanoparticles significantly influence the nanoparticle crystallinity, resulting into an altered phosphorescence of the nanomaterials.

On excitation at 325 nm laser radiations, we observed several sharp strong emission peaks among which peaks are very intense in the range 590–700 nm, coming from intra-4*f* transitions of $Pr^{3+}$ ions (Fig. 7a inset) [4, 7, 8]. The only significant change observed between these three samples in luminescent intensity, which improve after shell formation around the surface of core nanoparticles, is discussed in detailed later in this article. The emission observed is typical of the 4f - 4f rare earth transitions and is typical of $Pr^{3+}$ in a $[MoO_4]^{2-}$ environment. Under direct $4f^2 \rightarrow 4f^15d^1$ excitation of $Pr^{3+}$ around 325 nm, typical $4f^15d^1 \rightarrow 4f^2$ and $4f^2 \rightarrow 4f^2$ emissions of $Pr^{3+}$ were observed (Fig. 7a). Generally there are two possible 4f emitting states for the $Pr^{3+}$ ion, i.e. $^3P_0$ and $^1D_2$ levels, and the emission color of $Pr^{3+}$ depends on the intensity ratio of $4f^2 \rightarrow 4f^2$ transitions at a fixed energy, which is strongly affected by the host lattice. Typical $4f^2 \rightarrow 4f^2$ emission lines of $Pr^{3+}$ in the range of 480–800 nm are observed in the emission spectra, which can be assigned to $^3P_0 \rightarrow {}^3H_4$ (~500, 512 nm), $^3P_0 \rightarrow {}^3H_5$ (~595 nm),$^1D_2 \rightarrow {}^3H_4$ (~605 nm), $^3P_0 \rightarrow {}^3H_6$ (~624 nm), $^3P_0 \rightarrow {}^3F_2$ (~653 nm), $^3P_0 \rightarrow {}^3F_3$ (~693 nm) and $^3P_0 \rightarrow {}^3F_4$ (~736 nm) transitions, respectively [4, 7, 8]. However, a photon cascade emission ($^1S_0 \rightarrow {}^3P_1, {}^1I_6$ transitions) has not been observed, and is ascribed to the fact that the position of the lowest $4f^15d^1$ state (29 220 $cm^{-1}$) is lower than that of the $4f^2$ [$^1S_0$] level (46 800 $cm^{-1}$). On the other hand, as shown in Fig. 7a, typical $4f^15d^1 \rightarrow 4f^2$ and $4f^2 \rightarrow 4f^2$ emissions of $Pr^{3+}$ are observed under 325-nm excitation, which means that the energy transfer from the host lattice to $Pr^{3+}$ ions must be efficient. The strongest luminescence features are located at ~490, 605, and 652 nm which are ascribed to the $^3H_4 \rightarrow {}^3P_2$, $^1D_2 \rightarrow {}^3H_4$ and $^3P_0 \rightarrow {}^3F_2$ transitions, respectively. The observed emission for praseodymium ion-

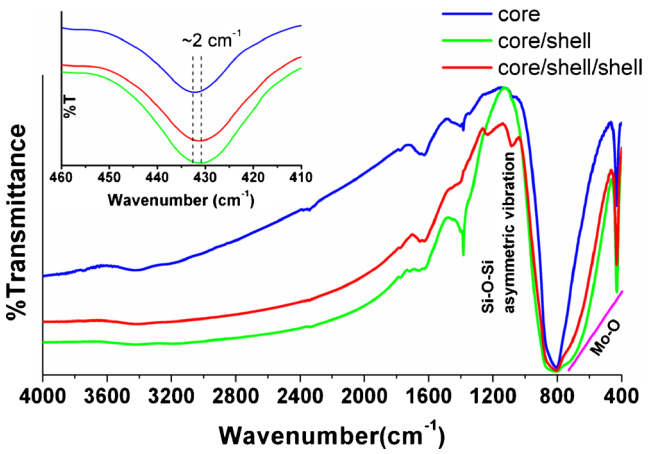


**Fig. 5** FTIR spectra of $CaMoO_4$:Pr (core), $CaMoO_4$:Pr@$CaMoO_4$ (core/shell) and $CaMoO_4$:Pr@$CaMoO_4$@$SiO_2$ (core/shell/shell) nanoparticles. Inset shows the expansion to stretching vibration of Mo-O ($A_u$ mode) between 460–410 $cm^{-1}$

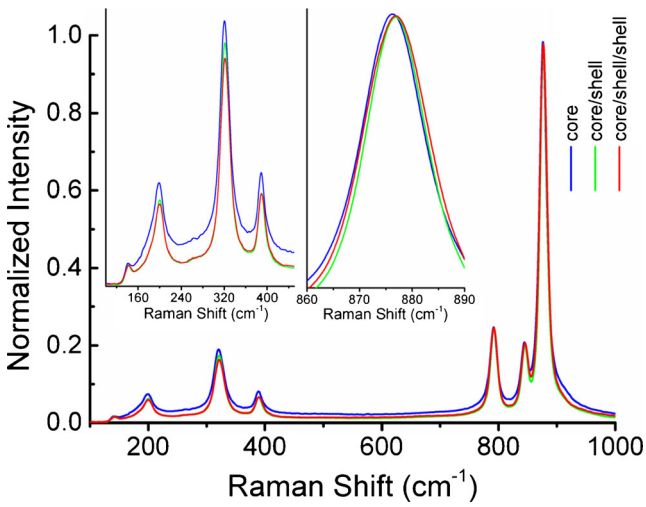


**Fig. 6** Normalized Raman spectrum of $CaMoO_4$:Pr (core), $CaMoO_4$:Pr@$CaMoO_4$ (core/shell) and $CaMoO_4$:Pr@$CaMoO_4$@$SiO_2$ (core/shell/shell) nanoparticles. Inset shows the expansion to spectrum between 100 to 450 $cm^{-1}$ and 860–890 $cm^{-1}$

**Table 2** Comparative experimental Raman-active modes results of $CaMoO_4$:Pr, $CaMoO_4$:Pr@$CaMoO_4$ and $CaMoO_4$:Pr@$CaMoO_4$@$SiO_2$ core-shell nanoparticles

| Samples | Bg(○) | Eg(★) | Eg(★) | Bg(●) | Ag(▼) | Eg(▼) | Ag(*) | Bg(▽) | Eg(♦) | Bg(♦) | Ag(♦) |
|---|---|---|---|---|---|---|---|---|---|---|---|
| $CaMoO_4$:Pr | ——— | ——— | 140 | 198 | 320 | ——— | 389 | ——— | 791 | 844 | 876 |
| $CaMoO_4$:Pr@ $CaMoO_4$ | ——— | ——— | 141 | 200 | 320 | ——— | 390 | ——— | 791 | 845 | 877 |
| $CaMoO_4$:Pr@ $CaMoO_4$@$SiO_2$ | ——— | ——— | 142 | 199 | 321 | ——— | 389 | ——— | 791 | 844 | 877 |

doped calcium molybdate nanoparticles is in agreement with the previously reported literature [7, 8].

The emission lines are sharp with multiple splitting, suggesting high crystallinity of the nanomaterials. They also indicate that surface modification with $CaMoO_4$ and silica shell affect the phase structure of the nanomaterials. The comparison of core and core-shell nanoparticles was done for the same weight percent of nanoparticles. Figure7b shows the integrated emission intensity of core, core/shell and core/shell/shell nanoparticles. On normalizing the emission intensity to that of the core nanoparticles, the emission intensity of core/shell and core/shell/shall intensity is found to be ~4.5 and 1.7 times of core nanoparticles. The observed maximum luminescence intensity for core/shell

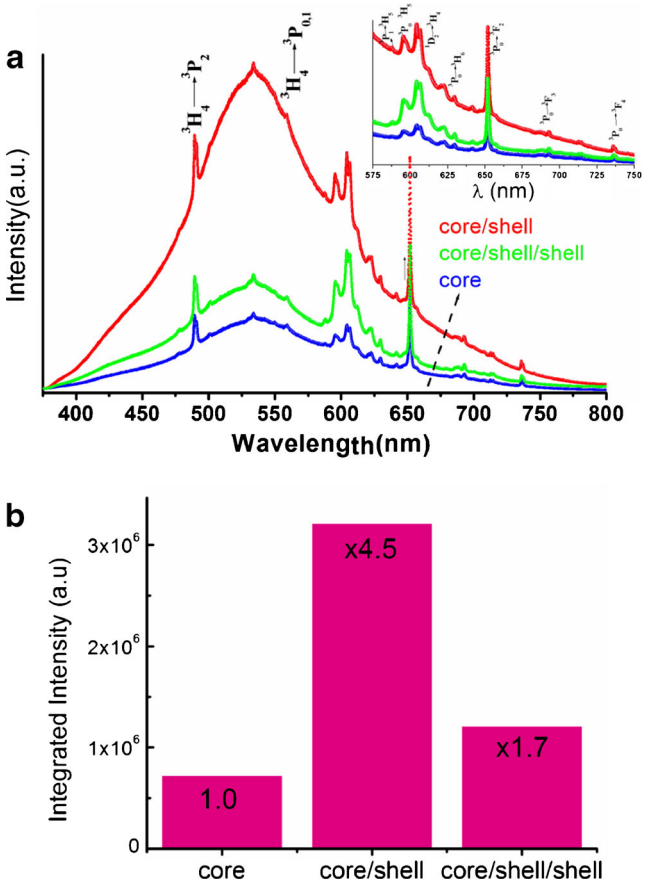


**Fig. 7** Emission spectrum of (**a**) $CaMoO_4$:Pr (core), $CaMoO_4$:Pr@$CaMoO_4$ (core/shell) and $CaMoO_4$:Pr@$CaMoO_4$@$SiO_2$ (core/shell/shell) nanoparticles under 325 nm laser excitation and (**b**) Compression of integrated emission intensity of the samples

($CaMoO_4$:Pr@$CaMoO_4$) nanoparticles in comparison with core $CaMoO_4$:Pr nanoparticles is attributed to the fact that a significant amount of nonradiative centers existing on the surface of $CaMoO_4$:Pr nanoparticles are eliminated by the shielding effect of the $CaMoO_4$ shell. In this core-shell structure, the distance between the luminescent lanthanide ions and the surface quenchers is increased, thus reducing the nonradiative pathways and suppressing the energy quenching in energy-transfer processes. Recently other researchers reported an improvement to the luminescence property with core–shell nanoparticles. Haase et al., were the first to report a quantum yield enhancement from 53 % for $CePO_4$:Tb nanoparticles to 80 % for $CePO_4$:Tb/$LaPO_4$ core–shell nanoparticles [29]. They attributed the significant enhancement of the quantum yield to a shell around each doped nanoparticle, which can suppress the energy-loss process on the particle surface. Veggel et al., ascribed the improved quantum yield of $LaF_3$/Ce,Te nanoparticles from 24 to 54 % to the $LaF_3$ shells around nanoparticles [30]. Yi et al., also reported a 7.4 and 29.6 times enhancements of the upconversion fluorescence intensities for $NaYF_4$:Yb/Er(Tm)/$NaYF_4$ core–shell nanoparticles, compared to non-coated samples [31]. They suggested that the emission intensity of the luminescent materials were improved to make a shell of suitable inorganic materials. Parchur et al. prepared $Tb^{3+}$ doped $CaMoO_4$ nonoparticles (core) and $CaMoO_4$ as shell (inactive) shows significant enhancement in luminescence intensity of core/shell structures [17]. In some case hetro-core-shell were prepared to enhance the luminescence intensity. Recently, Mao and his co-workers prepared $La_2Zr_2O_7$:$Eu^{3+}$@$YBO_3$ core@shell nanoparticles. $YBO_3$ shell formation over $La_2Zr_2O_7$:$Eu^{3+}$ core significantly enhances the luminescence intensity of electric dipole transition. These inorganic shell materials (homo/hetro materials as compared to core) reduce the nonradiative decay from defect centers on the surface of the nanoparticles. It means shell increases the distance between luminescent ion and quenching centers present on the surface of the sample [32]. The growth of a suitable inorganic material around each nanocrystal to form the core-shell structures has been regarded then as an effective strategy to improve luminescent efficiency.

After the core/shell nanoparticles were coated with a silica layer (~12 nm) their luminescence intensity decreased to some extent because of the light-scattering effect on both emission and incident light by the silica layer. Furthermore, the change of intensity between the non-silica coated sample and the silica-

coated sample can be explained by the changes of the of luminescent centers and there refractive index. The effective refractive index of the silica coated sample decreases compared to that of the non-silica coated sample giving rise to the decreased radiative transition rate. Additionally, the lower luminescence intensity of core/shell/shell ($CaMoO_4$:Pr@$CaMoO_4$@$SiO_2$) nanoparticles is caused by the absorption of silica in the UV region, which results in the decreased excitation intensity [33, 34]. As seen in Fig. 7a, no luminescent band of amorphous $SiO_2$ were detected due to the strong charge transfer band of the host material ($CaMoO_4$). However, after silica-shell formation around the surface of core/shell nanoparticles, most of the praseodymium ion emission transitions are found to be strongly perturbed, which could mean a broadening upon coordination with silica nanoparticles. These broadening in emission lines for silica coated core-shell nanoparticles suggest a decrease in the crystallinity of the material as compared to core and core/shell nanoparticles.

## Conclusions

Well-crystallized luminescent $CaMoO_4$:Pr (core), $CaMoO_4$:Pr@$CaMoO_4$ (core/shell) and $CaMoO_4$:Pr@$CaMoO_4$@$SiO_2$ (core/shell/shell) nanoparticles were successfully prepared by a polyol process. Our findings suggest that structural and optical properties of the nanomaterial are affected by shell formation around the surface of core nanoparticles. These results confirmed that $CaMoO_4$:Pr core and their core/shell nanoparticles are highly promising candidates for nanophosphor applications. These nanoparticles, ranging from 31 to 36 nm can be well dispersed in distilled water to form colloidal solutions. The calculated band gap which predicts the changes in band gap energy caused by the shell formation was confirmed by the UV/Vis results. As the band gap energy value varies with core/shell, the core and core/shell nanoparticles show characteristic charge-transfer broad greenish emission band of $[MoO_4]^{2-}$ and $Pr^{3+}$ ($4f^2 \rightarrow 4f^2$), respectively. The luminescent intensity of the core/shell ($CaMoO_4$:Pr@$CaMoO_4$) nanoparticles is greatly enhanced with respect to the core and core/shell/shell nanoparticles because the non-radiative processes at/near the surface of the nanoparticles are much reduced. These nanophosphor materials can be potentially used as labels for biological applications. Cytotoxixity and drug loading in core/shell/shell experiments are under investigation.

## References


1. Zhou J, Liu Z, Li F (2012) Upconversion nanophosphors for small-animal imaging. Chem Soc Rev 41(3):1323–1349
2. Ansari AA, Alam M, Labis JP, Alrokayan SA, Shafi G, Hasan TN, Alshatwi A (2011) Luminescent mesoporous $LaVO_4$:$Eu^{3+}$ core-shell nanoparticles: synthesis, characterization, biocompatibility and their cytotoxicity. J Mater Chem 21(48):19310–19316
3. Lin M, Zhao Y, Wang SQ, Liu M, Duan ZF, Chen YM, Li F, Xu F, Lu T (2012) Recent advances in synthesis and surface modification of lanthanide-doped upconversion nanoparticles for biomedical applications. Biotechnol Adv 30(6):1551–1561
4. Pelle F, Dhaouadi M, Michely L, Aschehoug P, Toncelli A, Veronesi S, Tonelli M (2011) Spectroscopic properties and upconversion in $Pr^{3+}$:$YF_3$ nanoparticles. Phys Chem Chem Phys 13(39):17453–17460
5. Lecointre A, Bessiere A, Bos AJJ, Dorenbos P, Viana B, Jacquart S (2011) Designing a red persistent luminescence phosphor: The example of YPO4:Pr3+, Ln3+ (Ln=Nd, Er, Ho, Dy). J Phys Chem C 115(10):4217–4227
6. Peng C, Li C, Li G, Li S, Lin J (2012) $YF_3$:$Ln^{3+}$ (Ln = Ce, Tb, Pr) sub microspindles: hydrothermal synthesis and luminescence properties. Dalton Trans 41(28):8660–8668
7. Tao F, Pan F, Wang Z, Cai W, Yao L (2010) Synthesis and photoluminescence properties of hexagonal Lanthanide(III)-doped $NaYF_4$ microprisms. CrystEngComm 12(12):4263–4267
8. Liu TC, Cheng BM, Hu SF, Liu RS (2011) Highly stable red oxynitride β-SiAlON:$Pr^{3+}$ phosphor for light-emitting diodes. Chem Mater 23(16):3698–3705
9. Marques VS, Cavalcante LS, Sczancoski JC, Alcantara AFP, Orlandi MO, Moraes E, Longo E, Varela JA, Li MS, Santos MRMC (2010) Effect of different solvent ratios (water/ethylene glycol) on the growth process of $CaMoO_4$ crystals and their optical properties. Crys Growth & Des 10(11):4752–4768
10. Longo VM, Cavalcante LS, Paris EC, Sczancoski JC, Pizani PS, Li MS, Andres J, Longo E, Varela JA (2011) Hierarchical assembly of $CaMoO_4$ Nano-octahedrons and their photoluminescence properties. J Phys Chem C 115(13):5207–5219
11. Raju GSR, Pavitra E, Ko YH, Yu JS (2012) A facile and efficient strategy for the preparation of stable $CaMoO_4$ spherulites using ammonium molybdate as a molybdenum source and their excitation induced tunable luminescent properties for optical applications. J Mater Chem 22(1):15562–15569
12. Ansari AA, Hasan TN, Syed NA, Labis JP, Parchur AK, Shafi G, Alshatwi A (2013) In-vitro cyto-toxicity, geno-toxicity and bio-imaging evaluation of one-pot synthesized luminescent functionalized mesoporous $SiO_2$@$Eu(OH)_3$ core-shell microspheres. Nanomed: Nanotech Biol and Med 9(2):1328–1332
13. Mahlik S, Behrendt M, Grinberg M, Cavalli E, Bettinelli M (2013) High pressure luminescence spectra of $CaMoO_4$:$Ln^{3+}$ (Ln = Pr, Tb). J Phys: Condens Matt 25(10):105502
14. Cavalli E, Boutinaud P, Mahiou R, Bettinelli M, Dorenbos P (2010) Luminescence dynamics in $Tb^{3+}$-Doped $CaWO_4$ and $CaMoO_4$ crystals. Inorg Chem 49(11):4916–4921
15. Vidya S, Solomon S, Thomas JK (2012) Synthesis, sintering and optical properties of $CaMoO_4$: A promising scheelite LTCC and photoluminescent material. Phys Status Solidi A 209(6):1067–1074
16. Parchur AK, Ningthoujam RS, Rai SB, Okram GS, Singh RA, Tyagi M, Gadkari SC, Tewari R, Vatsa RK (2011) Luminescence properties of $Eu^{3+}$ doped $CaMoO_4$ nanoparticles. Dalton Trans 40(29):7595–7601
17. Parchur AK, Prasad AI, Ansari AA, Raia SB, Ningthoujam RS (2012) Luminescence properties of $Tb^{3+}$-doped $CaMoO_4$ nanoparticles: annealing effect, polar medium dispersible, polymer film and core-shell formation. Dalton Trans 41(36):11032–11045
18. Mikhailik VB, Kraus H, Miller G, Mykhaylyk MS, Wahl D (2005) Luminescence of $CaWO_4$, $CaMoO_4$, and $ZnWO_4$ scintillating crystals under different excitations. J Appl Phys 97(8):083523
19. Mikhailik VB, Kraus H, Itoh M, Iri D, Uchida M (2005) High pressure luminescence spectra of $CaMoO_4$:$Ln^{3+}$ (Ln = Pr, Tb). J Phys Condens Matter 17(10):7209
20. Chung JH, Lee SY, Shim KB, Kweon SY, Ur SC, Ryu JH (2012) Blue upconversion luminescence of $CaMoO_4$:$Li^+$/$Yb^{3+}$/$Tm^{3+}$ phosphors prepared by complex citrate method. Appl Phys A 108(2):369

21. Ansari AA, Singh SP, Singh N, Malhotra BD (2012) Synthesis of optically active silica-coated $NdF_3$ core–shell nanoparticles. Spectrochim Acta Part A 86:432–436
22. Cavalcante LS, Sczancoski JC, Tranquilin RL, Joya MR, Pizani PS, Varela JA, Longo E (2008) $BaMoO_4$ powders processed in domestic microwave-hydrothermal: synthesis, characterization and photoluminescence at room temperature. J Phys Chem Solids 69(11):2674–2680
23. Yoon JW, Choi CJ, Kim D (2011) Laser-induced synthesis of $CaMoO_4$ nanocolloidal suspension and its optical properties. Mater Transac 52(4):768–771
24. Ansari AA, Singh N, Khan AF, Singh SP, Iftikhar K (2007) Solvent effect on optical properties of hydrated lanthanide tris-acetylacetone. J Lumin 127(2):446–452
25. Ansari AA, Labis JP (2012) One-pot synthesis and photoluminescence properties of luminescent functionalized mesoporous $SiO_2$@$Tb(OH)_3$ core-shell nanospheres. J Mater Chem 22(32):16649–16656
26. Tauc J, Menth A (1972) States in the gap. J Non-Cryst Solids 8(9): 569–585
27. Longo VM, de Figueiredo AT, Campos AB, Espinosa JWM, Hernandes AC, Taft CA, Sambrano JR, Varela JA, Longo E (2008) Different origins of green-light photoluminescence emission in structurally ordered and disordered powders of calcium molybdate. J Phys Chem A 112(38):8920–8928
28. Marques APA, Motta FV, Leite ER, Pizani PS, Varela JA, Longo E, de Melo DMA (2008) Evolution of photoluminescence as a function of the structural order or disorder in $CaMoO_4$ nanopowders. J Appl Phys 104(4):043505
29. Kompe K, Borchert H, Storz J, Lobo A, Adam S, Moller T, Haase M (2003) Green-emitting $CePO_4$:Tb/$LaPO_4$ core-shell nanoparticles with 70 % photoluminescence quantum yield. Angew Chem Int Edn 42(44):5513–5516
30. Stoudam JW, Veggel FCJMV (2004) Improvement in the luminescence properties and processability of $LaF_3$/Ln and $LaPO_4$/Ln nanoparticles by surface modification. Langmuir 20(26):11763–11771
31. Yi GS, Chow GM (2007) Water-soluble NaYF4:Yb, Er(Tm)/NaYF4/ polymer core/shell/shell nanoparticles with significant enhancement of upconversion fluorescence. Chem Mater 19(3):341–343
32. Alaparthi SB, Tian Y and Mao Y (2014) Synthesis and photoluminescence properties of $La_2Zr_2O_7$:$Eu^{3+}$@$YBO_3$ core@shell nanoparticles, Nanotechnology 25:025703(8 pp).
33. Mahalingam V, Vetrone F, Naccache R, Speghini A, Capobianco JA (2009) Colloidal $Tm^{3+}$/$Yb^{3+}$-Doped $LiYF_4$ nanocrystals:multiple luminescence spanning the UV to NIR regions via low-energy excitation. Adv Mater 21(40):4025–4028
34. Li Z, Zhang Y, Jiang S (2008) Multicolor core/shell-structured upconversion fluorescent nanoparticles. Adv Mater 20(24):4765–4769